



HAL
open science

Resilient high oxygen barrier multilayer films of nanocellulose and polylactide

Manon Guivier, Giana Almeida, Sandra Domenek, Chloé Chevigny

► To cite this version:

Manon Guivier, Giana Almeida, Sandra Domenek, Chloé Chevigny. Resilient high oxygen barrier multilayer films of nanocellulose and polylactide. *Carbohydrate Polymers*, 2023, 312, pp.120761. 10.1016/j.carbpol.2023.120761 . hal-04025312

HAL Id: hal-04025312

<https://hal.inrae.fr/hal-04025312>

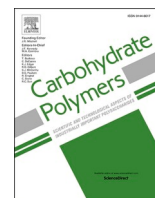
Submitted on 29 Mar 2023

HAL is a multi-disciplinary open access archive for the deposit and dissemination of scientific research documents, whether they are published or not. The documents may come from teaching and research institutions in France or abroad, or from public or private research centers.

L'archive ouverte pluridisciplinaire **HAL**, est destinée au dépôt et à la diffusion de documents scientifiques de niveau recherche, publiés ou non, émanant des établissements d'enseignement et de recherche français ou étrangers, des laboratoires publics ou privés.



Distributed under a Creative Commons Attribution - NonCommercial - NoDerivatives 4.0 International License



Resilient high oxygen barrier multilayer films of nanocellulose and polylactide

Manon Guivier, Giana Almeida, Sandra Domenek, Chloé Chevigny*

Université Paris-Saclay, INRAE, AgroParisTech, UMR SayFood, 22 Place de l'Agronomie, 91120 Palaiseau, France

ARTICLE INFO

Keywords:

Nanocelluloses
Polylactide
Multilayer films
High gas barrier properties

ABSTRACT

Nanocelluloses are promising high gas barrier materials for biobased food packaging, but they must be protected from water to preserve high performance. The respective O_2 barrier properties of different types of nanocelluloses were compared (nanofibers (CNF), oxidized nanofibers (CNF TEMPO) and nanocrystals (CNC)). The oxygen barrier performance for all types of nanocelluloses was similarly high. To protect the nanocellulose films from water, a multilayer material architecture was used with poly(lactide) (PLA) on the outside. To achieve this, a biobased tie layer was developed, using Corona treatment and chitosan. This allowed thin film coating with nanocellulose layers between 60 and 440 nm thickness. AFM images treated with Fast Fourier Transform showed the formation of locally-oriented CNC layers on the film. Coated PLA(CNC) films performed better ($3.2 \times 10^{-20} \text{ m}^3 \cdot \text{m/m}^2 \cdot \text{s} \cdot \text{Pa}$) than PLA(CNF) and PLA(CNF TEMPO) (1.1×10^{-19} at best), because thicker layers could be obtained. The oxygen barrier properties were constant during successive measurements at 0 % RH, 80 % RH and again at 0 % RH. This shows that PLA is sufficiently shielding nanocelluloses from water uptake to keep high performance in an extended range of RH and opens the way to high oxygen barrier films which are biobased and biodegradable.

1. Introduction

In recent years, growing needs in bio-based, biodegradable and renewable new materials gave rise to a strong interest in nanocellulose based materials (Ferrer et al., 2017; Lavoine et al., 2012; Nair et al., 2014). Nanocelluloses are obtained from plant fibers (wood, cotton...) without breaking down the individual cellulose nanofiber bundles and the crystalline structure of cellulose (Islam et al., 2014; Qing et al., 2013; Spence et al., 2011; B. Thomas et al., 2018). Cellulose nanocrystals (CNC) and cellulose nanofibers (CNF) properties are well documented in literature, particularly for food packaging applications (Hubbe et al., 2017; Islam et al., 2014; Lin & Dufresne, 2014; Nair et al., 2014; P. Thomas et al., 2020). Their bio-based and biodegradable character, transparency and high mechanical strength are especially useful in this application. Specifically, their very low oxygen permeability (around $10^{-23} \text{ m}^3 \cdot \text{m/m}^2 \cdot \text{s} \cdot \text{Pa}$ in a dry environment), allows them to protect food from oxidation, with a better performance than the most commonly-used petroleum-based perishable food packagings such as PET (polyethylene terephthalate) or EVOH (ethylene vinyl alcohol), which have

respective oxygen permeabilities of $1 \times 10^{-19} \text{ m}^3 \cdot \text{m/m}^2 \cdot \text{s} \cdot \text{Pa}$ and $6 \times 10^{-21} \text{ m}^3 \cdot \text{m/m}^2 \cdot \text{s} \cdot \text{Pa}$ (Lagaron et al., 2005; Lange & Wyser, 2003; Lavoine et al., 2012; Nair et al., 2014). This performance is linked to the high polarity of cellulose and the highly crystalline structure of nanocelluloses. Unfortunately, at high relative humidity (from 70 % and above), nanocelluloses swell and inter-fiber hydrogen bonds break, which is detrimental for the oxygen barrier properties. Therefore, one active field of study for nanocelluloses gas barrier applications have been in the enhancement of gas barrier properties at high relative humidity, notably by combining nanocelluloses with a hydrophobic polymer. Multilayered structures and coatings using apolar polymers were able to shield nanocelluloses from water vapor uptake (Martin & Jean, 2014). For example, Aulin et al. (2013) showed the positive effect of combining CNF/PEI coatings (using the Layer-by-Layer assembly technique) with PLA to reduce the oxygen permeability and water vapor permeability, and Lu et al. (2018) improved the barrier properties of biaxially oriented polypropylene/low density polyethylene (BOPP/LDPE) with a CNF layer applied by a plasma treatment and bar-coating.

Poly(lactide) (PLA) is a biodegradable polyester already used in food

* Corresponding author.

E-mail addresses: manon.guivier@agroparistech.fr (M. Guivier), giana.perre@agroparistech.fr (G. Almeida), sandra.domenek@agroparistech.fr (S. Domenek), chloe.chevigny@inrae.fr (C. Chevigny).

<https://doi.org/10.1016/j.carbpol.2023.120761>

Received 6 October 2022; Received in revised form 17 February 2023; Accepted 24 February 2023

Available online 3 March 2023

0144-8617/© 2023 The Authors. Published by Elsevier Ltd. This is an open access article under the CC BY-NC-ND license (<http://creativecommons.org/licenses/by-nc-nd/4.0/>).

packaging. While most commercial PLA is still fossil-based, it is possible to produce it from renewable biomass (starch, sugar). To increase its use in the food packaging sector, the poor gas barrier properties of PLA need to be enhanced. Previous work developing mainly nanocomposites underlined the ability of nanocelluloses to improve PLA gas barrier properties, without, however, reaching standard food packaging requirements (Espino-Pérez et al., 2018; Fortunati et al., 2012; Jung et al., 2020; Szymańska-Chargot et al., 2020). To overcome this issue, a change of architecture is necessary by creating a multilayered structure with at least two layers, one layer of PLA and one of nanocellulose. In the literature, only few studies report PLA/nanocelluloses (PLA(NC)) multilayered materials (Aulin et al., 2013; Koppolu et al., 2019; Le Gars, Dhuiège, et al., 2020; Martin & Jean, 2014). Different build-up processes were used: bar-coating, spin-coating, layer-by-layer assembly (Herrera et al., 2016; Le Gars, Dhuiège, et al., 2020; Martin & Jean, 2014; Spieser et al., 2020). Nanocelluloses are often modified to overcome their lack of adhesion with non-polar polymers (Espino-Pérez et al., 2018; Le Gars, Bras, et al., 2020; Mujica-García et al., 2016): the use of plasma treatment (Mirmehdi et al., 2018; Vartiainen et al., 2016) or adhesive layers (for example, acrylic resin, transparent polyurethane or cationic starch (Du et al., 2021; Koppolu et al., 2019; Wang et al., 2020)) are the most common ways to overcome the poor compatibility between the materials. Chitosan, a polysaccharide obtained by deacetylation of chitin (by-product of the crustacean industry), which is biocompatible and biodegradable, could be a better option. Indeed, chitosan is a cationic polysaccharide, able to form strong hydrogen and ionic interactions with the negatively charged nanocelluloses (Toivonen et al., 2015). Li et al. (2009) reported strong interactions between CNC and chitosan in nanocomposites, and good water resistance from such nanocomposite films.

Our main hypothesis is that multilayered high barrier performance materials using nanocelluloses can be made using only bio-sourced polymers. While nanocelluloses are obviously bio-sourced and biodegradable, previous works used either a fossil-based tie layer (acrylic, polyurethane, polyvinylalcohol), or a fossil-based hydrophobic protecting polymer (polypropylene, polyethylene), or both. Here PLA, which can be bio-sourced and is compostable, will be used as the protecting layer. To overcome the low adhesion of PLA and nanocelluloses, which was largely documented in studies on nanocomposites, chitosan is used as a tie layer, because of its positive charge likely to interact with negatively charged nanocelluloses and its possibility to orient and expose surfaces with high contact angle, observed in studies on free-standing chitosan films (Crouvisier-Urien et al., 2016). The oxygen barrier performance of this film architecture will be assessed both at 0 % relative humidity and at 80 % relative humidity. Furthermore, repeated testing at low, then high, and then again low RH will be carried out to investigate performance in service conditions of food packaging. We thus aim at demonstrating the potential for an entirely bio-sourced food packaging material, with functional high barrier performance, for the first time.

In this work, PLA/nanocellulose multilayer films were prepared using three different types of commercial nanocelluloses, CNC, CNF and CNF TEMPO. The adhesion of nanocelluloses on PLA film was optimized using Corona treatment and chitosan. The films were produced using a bar-coating process, mimicking industrial coating processes, and the oxygen barrier properties of the multilayer structures were assessed at different relative humidities.

2. Experimental section

2.1. Materials

Cellulose nanocrystals (CNC), cellulose nanofibers (CNF) and TEMPO-oxidized cellulose nanofibers (CNF TEMPO) were purchased as suspensions from the University of Maine (USA), with respective concentrations of 10.3 wt%, 3 wt% and 1.1 wt%. Those commercial

nanocelluloses have been extensively characterized by Jimenez-Saelices et al. (Jiménez Saelices & Capron, 2018): CNC were found to have average dimensions of $6.5 \times 20 \times 175 \text{ nm}^3$ and a negative surface charge (OSO_3^-) of $0.090 \pm 0.024 \text{ mmol/g}$, CNF an average diameter of 40 to 120 nm and a length of several micrometers, with no detectable surface charge, and CNF TEMPO have an average diameter of 3–8 nm, a length of several micrometers, and a negative surface charge (COO^-) of $1.084 \pm 0.04 \text{ mmol/g}$. These values are confirmed by other works (Nazari et al., 2016; Pignon et al., 2021). Medium molecular weight chitosan from deacetylated shrimp chitin (75–85 % deacetylation degree DD, molecular weight range: $(1.9\text{--}3.1) \times 10^5 \text{ Da}$), was purchased from Sigma-Aldrich (USA), with the supplier-given characteristics confirmed by the literature: DD 76 % (Ssekatawa et al., 2021) or 78 % (Vanden Braber et al., 2017), and molecular weight slightly above specifications but still within the same range: $361 \pm 32 \text{ kDa}$ (Ssekatawa et al., 2021) or $583 \pm 87 \text{ kDa}$ (Vanden Braber et al., 2017). Acetic acid (99 %–100 %) was purchased from Sigma-Aldrich (USA). Biaxially oriented PLA films (L-stereochemical form, density: 1.25 g.cm^{-3} , thickness 50 μm) were bought from Goodfellow (UK).

2.2. Production of multilayered films

2.2.1. Solution preparation

An aqueous solution of chitosan at 1 wt% was prepared with an addition of 1 wt% of acetic acid. The solution was maintained under stirring (500 rpm) for 4 h followed by an ultrasonic treatment (30 % amplitude, 5 min). CNC, CNF and CNF TEMPO suspensions were diluted to concentrations of 1 wt%, 0.05 wt% and 0.1 wt%, respectively. They were kept under agitation for 2 h at 500 rpm before an ultrasonic treatment (30 % amplitude, 5 min). Preliminary work permitted us to maximize nanocellulose concentrations avoiding aggregation during the coating process.

2.2.2. Bar coating

Chitosan and nanocellulose suspensions were coated using a bar-coater (Automatic Film Applicator, Industrial Physics, Netherlands). A 4 μm Mayer bar was selected to obtain nanometric layers. Coatings were executed with a bar speed of 30 mm.s^{-1} and a bed temperature of 40 °C.

2.2.3. Sample preparation

First, the PLA film was treated with a Corona treatment to enhance adhesion. A Mini Corona from Boussey-Control was used, with a frequency of 5 MHz, a voltage of 48 kV and a 6.5 cm length electrode. The chitosan solution was deposited on PLA, followed by nanocelluloses layers. Between each layer, samples were kept at 40 °C for at least 15 min to dry. Four films per nanocellulose type were prepared, with 2, 5, 8 and 10 deposits of nanocelluloses on a 1-layer-chitosan-coated PLA film. Samples are labelled according to the baseboard, nanocellulose type and number of deposits, such as $\text{PLA}(\text{nanocellulose type})_x$, where “PLA” is the baseboard, “nanocellulose type” refers to either CNC, CNF or CNF TEMPO and “x” refers to the number of nanocellulose deposits. Fig. 1 summarizes the samples. After the final coating, PLA(NC) films were dried at 40 °C under vacuum for 48 h, then stored in a desiccator over silica gel.

The theoretical thickness of chitosan/nanocellulose layer, coated over PLA, was computed according to Eq. (1):

$$L_{th} = C(\text{CS}) \times h_{\text{Mayer}} + C(\text{NC}) \times h_{\text{Mayer}} \times X, \quad (1)$$

where L_{th} is the theoretical thickness (nm), $C(\text{CS})$ and $C(\text{NC})$ are the concentration of chitosan and nanocellulose suspensions (wt%), h_{Mayer} the Mayer bar height (fixed at 4 μm) and X the number of deposits.

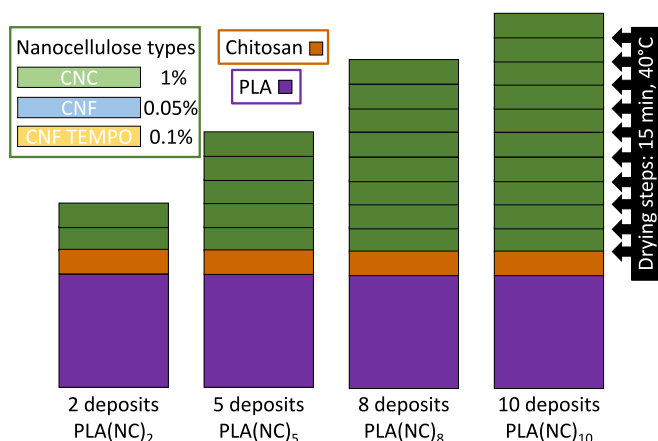


Fig. 1. Summary of sample structures.

2.3. Characterization methods

2.3.1. Water contact angle measurements

Water contact angle measurements were conducted using the sessile drop technique (KRUSS DSA 100 goniometer, France), under ambient conditions. Three to five water drops of 0.8 μL were deposited on each film, and the average water contact angle was calculated.

2.3.2. Scanning electron microscopy (SEM)

Scanning electron microscopy (SEM-FEG, FEI Quanta 250) was used to observe the cross-section of multilayered films. The samples were placed between 2 layers of rigid polystyrene (to maintain the sample flatness during the cut) and the whole system was cut with a microtome (UC6, Leica), to observe the corresponding cross-section. The following conditions were applied to obtain the images: an accelerating voltage of 2.5 kV, a spot size of 2.5 and a work distance of approximately 8 mm. This corresponds to a 3-nm resolution, roughly. The non-conductive samples were first coated with Au/Pd (5 nm layer) and partially covered with double sided carbon-tape. Images were analyzed with Gwyddion software (v 2.59) and thicknesses measured with ImageJ software (v 1.53 t).

2.3.3. Atomic force microscopy (AFM)

Tapping mode AFM images were collected using a multimode microscope controlled by Veeco Nanoscope V controller. The AFM cantilever (silicon, spring constant of 40 N/m, oscillation frequency of 300 kHz) had a radius curvature under 10 nm. Images of the sample surfaces were collected in air under ambient conditions. Sample roughness was averaged from 12 measurements over 1 $\mu\text{m} \times 1 \mu\text{m}$ images. AFM images were analyzed with Gwyddion software and its Fast Fourier Transform (FFT) function was utilized to convert AFM images into mathematically defined frequency space. FFT images contain gray-scale pixels and emphasize the degree of alignment present in the AFM images. A round FFT pattern corresponds to a lack of orientation in the initial AFM image, whereas elongated FFT pattern indicates an orientation. In the case of oriented samples, the elongated FFT pattern form an angle of 90° with the actual orientation direction of the sample. Similar analyses were performed with CNF sprayed layers by Blell et al. (2017).

The thickness of CS/NC layer in ambient conditions was determined by AFM scratch height measurements, with a protocol adapted from Cranston and Gray (2008). AFM images and scratching were performed in contact mode (PicoLE, Molecular Imaging, ScienTec), with a NSC 15/AL cantilever from MikroMasch (silicon, spring constant of 40 N/m, oscillation frequency of 325 kHz, radius curvature of 8 nm). A constant resolution of 512 pixels \times 512 pixels was used and an optimum set point of 2.5 V was fixed. According to preliminary height scratch measurements, a set point under 2.5 V was not able to remove efficiently the CS/

NC layer and a set point above 2.5 V damaged the PLA surface. Scratching was realized over a 1 $\mu\text{m} \times 1 \mu\text{m}$ surface and the sample was reimaged (10 $\mu\text{m} \times 10 \mu\text{m}$) in contact mode. The CS/NC layer height was obtained by averaging 6 profile analyses of the scratch area (by taking the scratch area and the top of the film). Images were analyzed with Gwyddion software.

2.3.4. Dynamic vapor sorption

A dynamic vapor sorption (DVS) from Surface Measurement Systems (UK) was employed to determine the water sorption behavior of multi-layered films. It has a relative precision of 0.1 μg ($\pm 1\%$). A specific pan was designed to optimize the contact surface between the sample and the water vapor. Measurements were performed under a continuous flow of nitrogen, at 25 °C. A three steps program was carried out, with a first step at 0 % RH for 1440 min (1 d), to reach an equilibrium and determine the anhydrous film mass. Then, a second step at 30 % RH for 2880 min (2 d) and a third step at 80 % RH for 4320 min (3 d) were realized. The duration of each step was optimized by Espino-Pérez et al. (2018), with the equilibrium criterium after each step being dm/dt lower than 0.001 %/min. PLA(NC) film samples had a mass between 25 and 30 mg. CNF TEMPO coated samples were replicated to check repeatability and experimental error.

The moisture content on a dry basis (MC) was calculated for each sample (corresponding to the water adsorbed), according to Eq. (2):

$$MC(sample) = \frac{m_{humid} - m_{dry}}{m_{dry}} \times 100, \quad (2)$$

where $MC(sample)$ is the moisture content of the sample (%), m_{humid} the sample mass in humid environment after reaching an equilibrium (g) and m_{dry} the anhydrous sample mass (g).

The theoretical moisture content of the film samples was calculated, on the hypothesis of additivity of individual moisture content of PLA, chitosan and nanocelluloses layers. The bulk chitosan moisture content (17 $\text{g}_{\text{water}}/\text{100g}_{\text{dry}}$ basis at 74 % RH) was obtained from Despond et al. (2001), who studied the water sorption of chitosan solvent-casted film at different RH. Consequently, the theoretical moisture content ($MC(sample)_{th}$) was obtained using Eq. (3):

$$MC(sample)_{th} = \frac{m(PLA) * MC(PLA) + m(CS) * MC(CS) + m(NC) * MC(NC)}{m(sample)}, \quad (3)$$

where $MC(PLA)$, $MC(CS)$, $MC(NC)$ are the moisture content of pure PLA, bulk chitosan film and bulk nanocelluloses films ($\text{g}_{\text{water}}/\text{100g}_{\text{dry}}$ basis) and $m(PLA)$, $m(CS)$, $m(NC)$, the respective mass PLA, chitosan and nanocelluloses layers and $m(sample)$ the sample mass (g).

2.3.5. Oxygen permeability at controlled relative humidity conditions

An in-house bubbler system equipped with a gas permeation cell, from PreSens Precision Sensing GmbH (Germany), was utilized in order to characterize the oxygen barrier properties in controlled relative humidity conditions (Fig. 2a,b). The PreSens cell measurement is based on the detection of O_2 molecules by fluorescence with an optical sensor. The relation between the O_2 concentration and luminescence is determined according to the Stern-Volmer equation (Eq. (4)):

$$\frac{\tau_0}{\tau} = 1 + k_{sv} \times [O_2], \quad (4)$$

where τ_0 and τ are the luminescence decay times in absence and presence of oxygen (s), k_{sv} is the overall Stern-Volmer quenching constant (ppm) and $[O_2]$ is the oxygen concentration (ppm).

Dry measurements were realized at 23 °C and 0 % RH according to ASTM D 3985. First, a dry nitrogen flow was brought to both chambers during 15 min to evacuate residual oxygen molecules. Then the bottom chamber was filled with dry oxygen gas for 1 min (Fig. 2c) and the experiment started (after closing the cell valves). The measurements

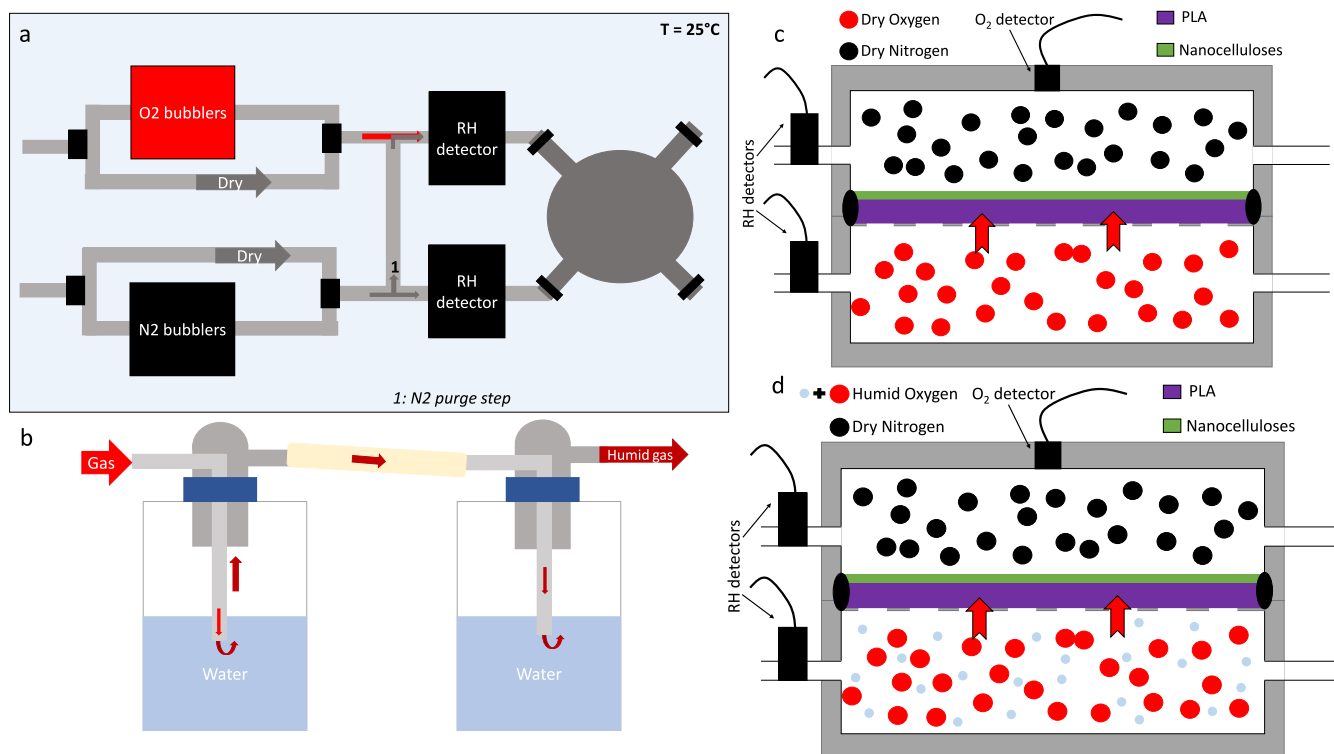


Fig. 2. In-house bubblers system with a PreSens cell (a), O₂ and N₂ bubblers set-up (b) and PreSens chambers during measurements in dry conditions (dry nitrogen and oxygen) (c) and in dry-humid conditions (dry nitrogen and humid oxygen) (d).

were executed under static conditions, due to the high barrier properties of the samples. Three to five replicates were analyzed.

Measurements in “dry-humid” conditions were performed as follows. Dried nitrogen flushed both chambers for 15 min. Then, the dry nitrogen flow was kept in the upper chamber, whereas humid oxygen flow was applied to the bottom chamber (PLA side of the film) (Fig. 2d). Oxygen gas was humidified with an in-house bubbler system, illustrated in Fig. 2b. After 1 min, the humid oxygen reached 80 % (± 3 %) relative humidity (RH), the chamber valves were closed and the experiment started. Each experiment was performed for at least 2 h. Three replicates were characterized in dry-humid environment.

Measurements in humid conditions were done by humidifying N₂ and O₂ with the in-house bubbler systems (Fig. D, supporting information). Humid nitrogen was brought to both chambers for 15 min, then humid oxygen was applied in upper chamber, for 1 min. The relative humidity of both gases reached 80 % (± 3 %). The experiments were performed on 2 replicates and for 2 h. In the aim to investigate the effect of repeated humidifying/drying cycles on the barrier properties, the measured films were stored in desiccator for 24 h to remove water and then measured again.

The oxygen transmission rate (OTR) was determined according to Eq. (5) and the final oxygen permeation was estimated according to Eq. (6):

$$OTR = \frac{dP_{O_2}}{dt} \frac{V_{cell} \times T_{std}}{P_{std} \times A \times P_m \times T_m}, \quad (5)$$

$$OP = OTR \times L, \quad (6)$$

where dP_{O_2}/dt is the evolution of oxygen partial pressure in the upper chamber ($\text{Pa} \cdot \text{s}^{-1}$). V_{cell} is the volume of the upper chamber ($1.1 \times 10^{-4} \text{ m}^3$) and A is the permeation area ($6.81 \times 10^{-3} \text{ m}^2$). P_{std} and P_m are the standard pressure (1.013 $\times 10^5$ Pa) and the average atmospheric pressure (Pa) during measurement, respectively. T_{std} and T_m are the standard temperature (273 K) and the average ambient temperature (K) during measurement, respectively. L is the film thickness (m), measured with a

Minigauge (ElektroPhysik, Germany). The oxygen permeability (OP) is given in SI units ($\text{m}^3 \cdot \text{m} / \text{m}^2 \cdot \text{s} \cdot \text{Pa}$).

To understand the effect of coatings and compare the nanocelluloses types, the normalized oxygen permeation of chitosan/nanocellulose (CS/NC) layer was calculated, according to Eq. (7):

$$\frac{L(sample)}{OP(sample)} = \frac{L(CS/NC)}{OP(CS/NC)} + \frac{L(PLA)}{OP(PLA)}, \quad (7)$$

where $L(sample)$, $L(CS/NC)$ and $L(PLA)$ are the sample, PLA layer and CS/NC layer thicknesses, respectively. $OP(sample)$, $OP(CS/NC)$ and $OP(PLA)$ are their respective oxygen permeation values.

3. Results and discussion

3.1. Characterization of nanocellulose layer

The coated PLA films were transparent and shiny, no visual difference to pure PLA film was observed (Fig. A, supporting information). To increase the adhesion between PLA and nanocelluloses, a pre-treatment was used, consisting in a Corona treatment and a pre-coating with chitosan prior to nanocelluloses deposition. Fig. 3a shows the water contact angle of pure PLA, Corona treated PLA and Corona treated PLA with a chitosan layer. Their respective water contact angles were: $63.6 \pm 1.1^\circ$, $38.5 \pm 1.7^\circ$ and $8.2 \pm 0.5^\circ$. Corona treatment is commonly used to enhance the surface polarity and roughness of PLA, to increase the adhesion of a coating layer (Rocca-Smith, 2016). Chitosan polar structure, with free hydroxyl groups able to form hydrogen bonds with water molecules, explains the water contact angle reduction for chitosan-coated PLA. Furthermore, chitosan carries a positive surface charge. Hence, Corona treatment and chitosan coating were able to decrease by 87 % the water contact angle and allow a more homogeneous coating of nanocelluloses on PLA. Nanocelluloses also have a high number of free hydroxyl groups and carry an overall negative surface charge, which efficiently creates hydrogen bonds and ionic interactions with chitosan

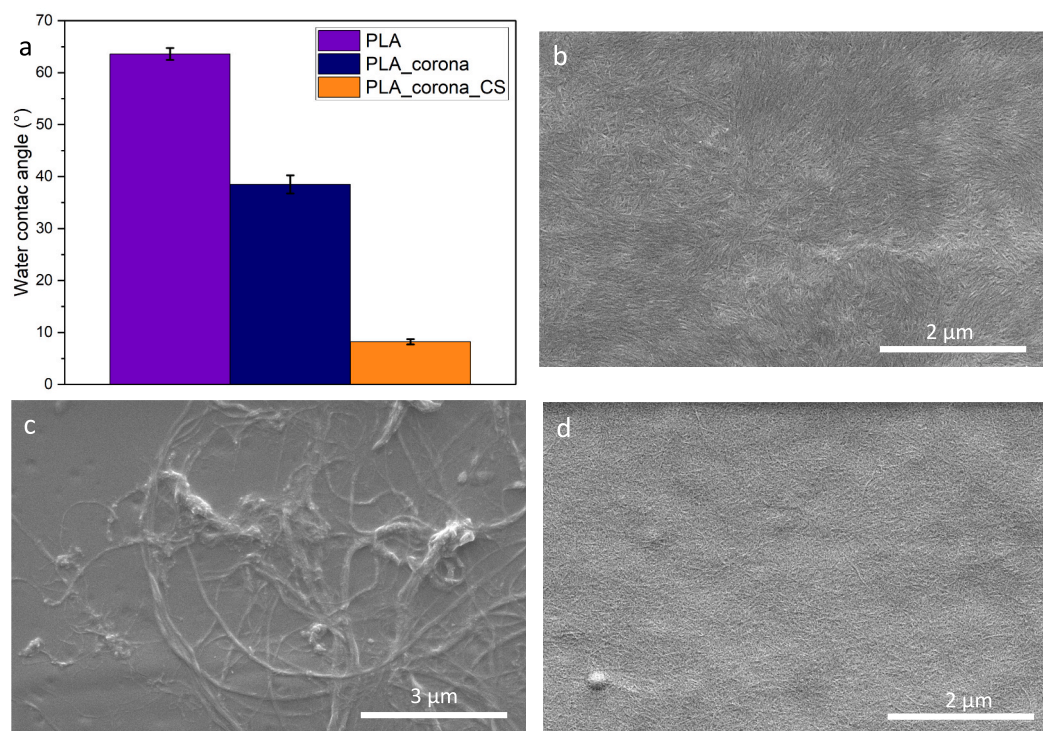


Fig. 3. Water contact angle measurements on pure PLA, Corona treated PLA and Corona treated PLA coated with a chitosan layer (a), SEM surface images of PLA (CNC)₁₀ (b), PLA(CNF)₁₀ (c), PLA(CNF TEMPO)₁₀ (d) samples.

(Toivonen et al., 2015). Fig. 3b, c and d show the SEM observed surface images of PLA films coated with nanocelluloses. CNC and CNF TEMPO coated films images display a homogeneous deposition of nanocelluloses over PLA surfaces. No holes are observed. However, entangled fibers are noticed for CNF coating, due to aggregates, even at low concentration. These SEM images confirm the difficulty to deposit CNF suspensions even at very low concentration. Of all three nanocelluloses types, CNF is the only one without a detectable charge, which might be another explanation for the more difficult deposit here. More in-depth measurements of the films, like surface charge, could help better understand the deposit adhesion mechanism.

Table 1 reports theoretical thicknesses of all chitosan/nanocellulose layers (CS/NC) (from Eq. (1)) and experimental thicknesses extracted from SEM observations of all cross-section films (Fig. B, supporting information). SEM images were focused on the PLA side coated with CS/NC layer, in order to estimate its thickness. The average thickness of CS/NC layer was calculated for each film, from 5 images (8 to 10 measurements per image) with ImageJ software. The resulting thicknesses (Table 1) are slightly above the theoretical values, due to the limitation of the resolution of SEM images. To overcome the lack of accuracy in the thickness determination with SEM, a second characterization was performed with atomic force microscopy (AFM).

Table 1 and Fig. 4 present the CS/CNC thicknesses determined by

AFM using the height scratching protocol adapted from Cranston and Gray (2008). Fig. 4 shows the effect of scratching on the surface and the corresponding height profile of the scratched area. The thicknesses of CS/NC layers, from the height scratch method, were close to the theoretical thicknesses, in the case of CNF and CNF TEMPO coatings. In the case of PLA(CNC)₂ the sample thickness obtained with height scratching was lower than the theoretical thickness showing that the coated materials was partially removed, and in the case of PLA(CNC)₁₀, scratching was not even possible with the present methodology. It appears that adhesion between the CS/CNC layer and PLA is much stronger than for other nanocelluloses type, and increases with the number of deposits. Possibly also there could be a thickness limit for successful scratching. The multiple deposits and bar-coating process might improve the CNC arrangements and create a more compact layer.

AFM measurements were also used to determine the average roughness of samples, as summarized in the Table 1. The coating layer should minimize the PLA roughness by filling its porosities, according to Yoox et al. and Gicquel et al. (Gicquel et al., 2017; Yook et al., 2020). The pre-coating treatment, based on a 40 nm thick layer of chitosan, was able to fill PLA porosities because of its dimensions. Consequently, the sample roughness on Table 1 corresponds to the nanocellulose layer roughness.

PLA(CNC) samples roughness are divided by 2 compared to pure

Table 1

Chitosan/nanocellulose thicknesses obtained by calculation, SEM, AFM height scratching and their corresponding average roughness.

Sample	CS/NC theoretical thickness (nm)	CS/NC thickness from SEM (nm)	CS/NC thickness from AFM (nm)	AFM average roughness (nm)
PLA	–	–	–	8.1 ± 2.1
PLA(CNC) ₂	120	197 ± 36	66 ± 24	4.9 ± 1.1
PLA(CNC) ₁₀	440	468 ± 60	No scratch ^a	4.7 ± 0.5
PLA(CNF) ₂	44	262 ± 69	48 ± 17	18.4 ± 9.1
PLA(CNF) ₁₀	60	138 ± 34	70 ± 11	10.5 ± 2.7
PLA(CNF T) ₂	48	61 ± 18	52 ± 7	6.5 ± 0.8
PLA(CNF T) ₁₀	80	100 ± 32	141 ± 22	5.2 ± 2.1

^a Impossible to scratch the CS/NC layer.

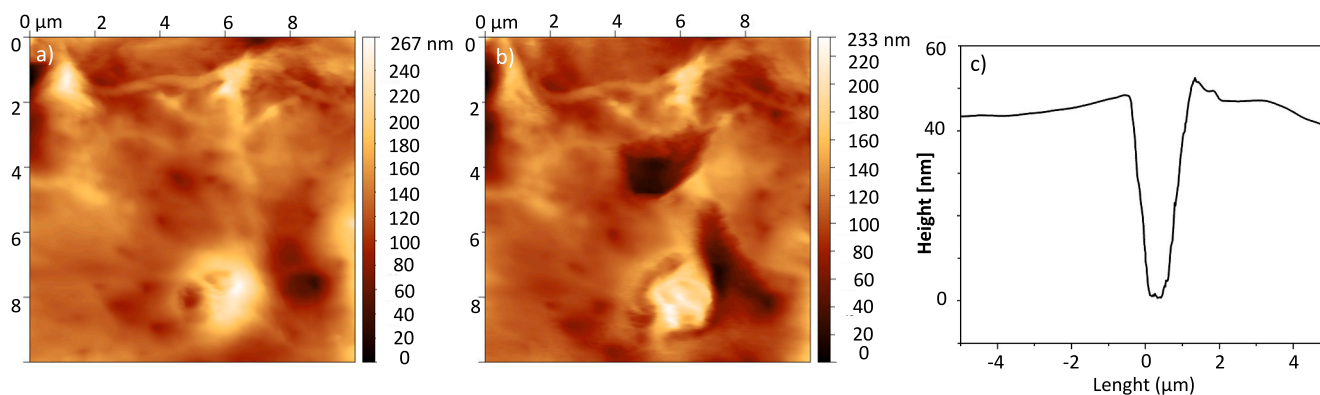


Fig. 4. AFM height images of PLA(CNF)₂ film (a), scratched PLA(CNF)₂ film (b) and its corresponding profile analysis (c).

PLA. CNF TEMPO coatings also reduce the sample roughness. On the other hand, CNF-coated samples are rougher than pure PLA. The nanofiber dimensions (200 to 800 nm length) and their strong interactions can explain their ability to form a highly entangled network, but also to form fiber aggregates, increasing the roughness. Moreover, increasing the number of deposits decrease the sample roughness, for each nanocellulose type. This reduction can be related to the successive addition of nanocellulose materials, which fills the porosities of the previous deposits and improves the coating layer homogeneity.

3.2. Orientation of nanocelluloses

AFM images were employed to analyze the surface structure and orientation of nanocelluloses, as observed in Fig. 5. On each image, the nanocelluloses coating is visible and homogeneous, the surface of PLA is completely covered without holes.

Fast Fourier Transform (FFT) images were used to investigate the orientation of nanocelluloses; 5 to 8 images were analyzed on different part of each film. CNC-coated films with 2 and 10 deposits showed a specific arrangement along the arrows (Fig. 5a, b). The small dimensions of CNC and their ability to be oriented through different methods, as suggested by literature (Cranston & Gray, 2006; Du et al., 2020, 2021; Revol et al., 1992; Yoshiharu et al., 1997), can be correlated to the orientation noticed in our work. The orientation increased with the

number of deposits, leading to the hypothesis that successive bar-coating depositions are able to rearrange CNC. Previous investigations of CNC orientation were performed by AFM (Cranston & Gray, 2006; Du et al., 2021), but in absence of FFT characterization, the occurrence of orientation could not be supported by the experimental evidence. Indeed, Blell et al. (2017) pointed out the importance of FFT to characterize the orientation on AFM images. In our work, FFT confirms the CNC orientation on PLA(CNC)₁₀ sample in local clusters with an average size of 1 μm. Further images can be found in the supporting information (Fig. C).

Fig. 5c, d, e and f represent CNF and CNF TEMPO-coated samples. A dense and entangled network was formed by the nanofibers, ensuring a homogeneous coverage of PLA without orientation, as confirmed by FFT. Entangled nanofibers are clearly distinguishable on Fig. 5c and d, without affecting the homogeneous coverage of PLA surfaces. Fig. 5e and f show that CNF TEMPO had smaller dimensions, but orientation was only achieved with CNC.

3.3. Barrier properties

3.3.1. Water sensitivity of nanocelluloses

Because of the high-water sensitivity of nanocelluloses, it is important to characterize their water vapor sorption behavior. Fig. 6 and Table 2 present the experimental data on water vapor sorption kinetics

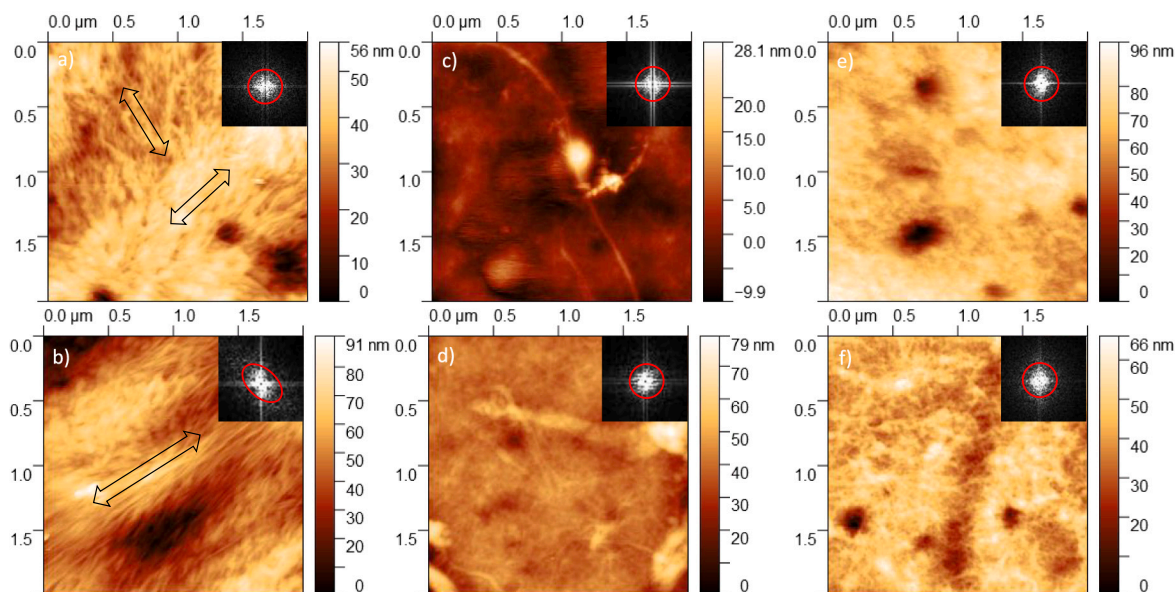


Fig. 5. AFM height images of PLA(CNC)₂ (a), PLA(CNC)₁₀ (b), PLA(CNF)₂ (c), PLA(CNF)₁₀ (d), PLA(CNF T)₂ (e), PLA(CNF T)₁₀ (f) and their corresponding Fast Fourier Transform images.

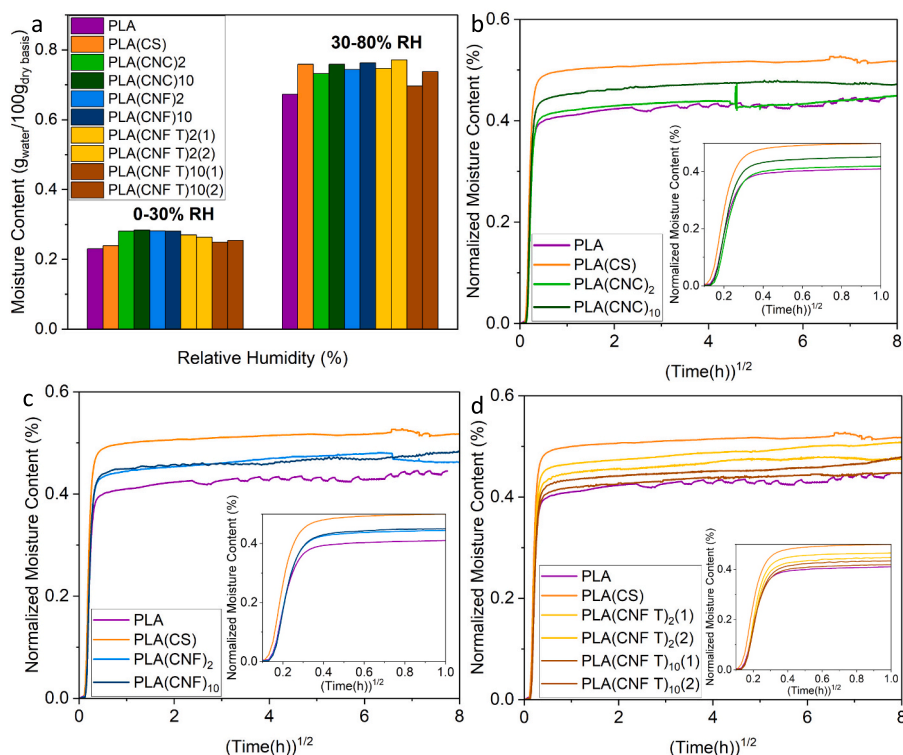


Fig. 6. Moisture content of uncoated and coated PLA at 30 % and 80 % relative humidity (a), the corresponding normalized moisture content curves for the 30–80 % RH step with CNC coatings (b), CNF coatings (c) and CNF TEMPO coatings (d) acquired with dynamic vapor sorption measurements. Inserts correspond to magnified view of the early time data.

Table 2

Thickness of PLA, bulk NC and CS/NC layers and the sample moisture content (MC) at 30 % RH and 80 % RH with the corresponding theoretical moisture content at 80 % RH. Experimental variability: 10 %.

Samples	Thickness		MC (sample) ($g_{water}/100g_{dry}$ basis)		MC(sample) _{th} ($g_{water}/100g_{dry}$ basis) ^a
	PLA and bulk NC (μm)	CS/NC layer (nm)	30 % RH	80 % RH	80 % RH
CNC	120 ± 11	–	3.28	11.9	–
CNF	95 ± 13	–	4.45	13.08	–
CNF TEMPO	85 ± 6	–	4.98	20.09	–
Chitosan (Despond et al., 2001)	20	–	3.8 (24 % RH)	17 (74 % RH)	–
PLA	50 ± 2	–	0.23	0.673	–
PLA(CS)	50 ± 2	40	0.239	0.759	0.675
PLA(CNC) ₂	50 ± 2	120	0.284	0.73	0.697
PLA(CNC) ₁₀	50 ± 2	440	0.284	0.759	0.782
PLA(CNF) ₂	50 ± 2	44	0.281	0.744	0.677
PLA(CNF) ₁₀	50 ± 2	60	0.281	0.763	0.682
PLA(CNF T) ₂ (1)	50 ± 2	48	0.27	0.747	0.679
PLA(CNF T) ₂ (2)	50 ± 2	48	0.263	0.771	0.679
PLA(CNF T) ₁₀ (1)	50 ± 2	80	0.249	0.697	0.694
PLA(CNF T) ₁₀ (2)	50 ± 2	80	0.254	0.738	0.694

^a Applying Eq. (3).

(30–80 % RH step) and the equilibrium moisture content at 30 % RH and 80 % RH.

In Fig. 6, coated PLA films showed higher moisture content uptake compared to uncoated PLA film, at both RH. However, due to the large

thickness of the PLA film ($(50 \pm 2) \mu m$) compared to the thickness of coatings (from 40 to 440 nm, see Table 2) the differences were relatively small: the smallest differences were obtained between PLA and PLA(CNF T)₁₀(1) (184 μg and 241 μg at 30 % RH and 80 % RH, respectively) and the highest between PLA and PLA(CNC)₁₀ (534 μg and 863 μg at 30 % RH and 80 % RH, respectively). No influence of the nanocellulose type (CNC, CNF or CNF TEMPO) on the water sensitivity was reliably found, because no significant differences (variability of 10 %) in water moisture content behavior were observed at both RH. The high affinity of chitosan to water vapor observed in previous work (Despond et al., 2001) is confirmed by our results: when relative humidity increased from 30 % to 80 %, PLA(CS) film absorbed 862 μg more than the uncoated PLA film.

The influence of the number of deposits was also checked. CNC samples showed a slight increase in water sensitivity when the number of deposits increased from 120 to 440 nm (mass uptake differences of 0.26 μg) (Fig. 6a, b). Samples with 10 layers of CNC simply contained more nanocelluloses, and thus were able to absorb more water. Concerning CNF and CNF TEMPO-coated samples, the presence of nanofibers aggregates and the small thickness differences between 2 and 10 deposits (16 nm and 32 nm for CNF and CNF TEMPO coatings, respectively) did not allow to observe differences on their water vapor adsorption as a function of the number of deposits.

In order to study the effect of each type of layer on the hygroscopicity of the multilayer film, the moisture content of bulk nanocellulose films were calculated, as presented in Table 2. The bulk moisture content of each layer was used to calculate the theoretical moisture content of the coated-PLA films at 80 % RH (Eq. (3)). The comparison between theoretical and experimental moisture contents, shown in Table 2, showed higher experimental moisture contents as compared to theoretical values (0.4 to 13.5 %). The differences between theoretical and experimental moisture contents can be related to the swelling of thin films of nanocellulose. As shown by Espino-Pérez et al. (2016), nanocelluloses swell when exposed to moisture and swelling induces non-Fickian diffusion. When the film thickness decreased (from bulk film to a

nanometric-coated layer), the non-Fickian influence is more noticeable (Almeida et al., 2020). The equilibrium masses obtained in the thin films might therefore be higher because of the contribution of non-Fickian transport. Additionally, the difficulty to obtain the exact experimental CS/NC layer thicknesses introduced an incertitude concerning the computed theoretical values, as the use of bulk chitosan value from literature did. Despite this incertitude, the differences between the experimental and theoretical moisture contents were relatively small, confirming the additive water sorption behavior of each layer, in the case of a multilayer architecture.

3.3.2. Oxygen barrier properties of PLA films coated with different types of nanocelluloses

The oxygen permeability of samples was characterized to identify the impact of nanocellulose coatings on PLA barrier properties. Nanocelluloses have outstanding oxygen barrier properties, reaching the performances of high barrier polymers such as ethyl vinyl alcohol employed in the food packaging industry (Lavoine et al., 2012; Nair et al., 2014). Table 3 summarizes the oxygen permeabilities of the samples, measured in dry conditions. Using Eq. (7), the specific oxygen permeability of the chitosan/nanocellulose (CS/NC) barrier layer was calculated and reported in the same Table 3.

The oxygen permeability of pure PLA film ($(1.80 \pm 0.01) \times 10^{-18} \text{ m}^3 \cdot \text{m} / \text{m}^2 \cdot \text{s} \cdot \text{Pa}$) (Table 3) was comparable to literature values (Colomines et al., 2010; Courgneau et al., 2012; Le Gars, Dhuiège, et al., 2020). After a first coated layer of chitosan, the oxygen permeability decreased by a factor 2, reaching a value comparable to the most favorable PLA/nanocelluloses bulk nanocomposites⁵⁰ ($(7.6 \pm 1.1) \times 10^{-19} \text{ m}^3 \cdot \text{m} / \text{m}^2 \cdot \text{s} \cdot \text{Pa}$). CNF and CNF TEMPO coatings decreased the oxygen permeability of the PLA-based samples by one order of magnitude and CNC coatings even by two orders of magnitude (Table 3). Chitosan and nanocelluloses 2D-coatings are highly performing in the multilayer architecture.

The oxygen transfer rate depends on the thickness of the barrier coating. In the case of very thin films, their barrier properties can be underperforming because of flaws and changes in the materials

Table 3

Comparison of oxygen permeability of the entire film (OP(sample)) and calculated oxygen permeability of the chitosan/nanocellulose (CS/NC) barrier layer (0 % RH, 23 °C).

Samples	CS/NC layer theoretical thickness (nm)	OP(sample) ($\text{m}^3 \cdot \text{m} / \text{m}^2 \cdot \text{s} \cdot \text{Pa}$)	OP(CS/NC) ($\text{m}^3 \cdot \text{m} / \text{m}^2 \cdot \text{s} \cdot \text{Pa}$)
PLA	–	$(1.8 \pm 0.01) \times 10^{-18}$	X
PLA(CS)	40	$(7.6 \pm 1.1) \times 10^{-19}$	$(1.1 \pm 0.4) \times 10^{-21}$
PLA (CNC) ₂	120	$(4.2 \pm 1) \times 10^{-20}$	$(7.4 \pm 0.2) \times 10^{-22}$
PLA (CNC) ₅	240	$(5.2 \pm 3.8) \times 10^{-20}$	$(2.5 \pm 1.9) \times 10^{-22}$
PLA (CNC) ₈	360	$(3.2 \pm 2) \times 10^{-20}$	$(2.4 \pm 1.5) \times 10^{-22}$
PLA (CNC) ₁₀	440	$(4.6 \pm 0.8) \times 10^{-20}$	$(3.1 \pm 1.8) \times 10^{-22}$
PLA(CNF) ₂	44	$(2.8 \pm 0.3) \times 10^{-19}$	$(3 \pm 0.4) \times 10^{-22}$
PLA(CNF) ₅	50	$(2.6 \pm 0.1) \times 10^{-19}$	$(3 \pm 0.1) \times 10^{-22}$
PLA(CNF) ₈	56	$(2.2 \pm 0.2) \times 10^{-19}$	$(2.9 \pm 0.3) \times 10^{-22}$
PLA (CNF) ₁₀	60	$(1.3 \pm 0.1) \times 10^{-19}$	$(1.7 \pm 0.1) \times 10^{-22}$
PLA(CNF T) ₂	48	$(8 \pm 1.7) \times 10^{-19}$	$(1.4 \pm 0.5) \times 10^{-21}$
PLA(CNF T) ₅	60	$(4.7 \pm 3.9) \times 10^{-19}$	$(1.4 \pm 0.9) \times 10^{-21}$
PLA(CNF T) ₈	72	$(3 \pm 1.7) \times 10^{-19}$	$(7.3 \pm 2.7) \times 10^{-22}$
PLA(CNF T) ₁₀	80	$(1.1 \pm 0.1) \times 10^{-19}$	$(1.9 \pm 0.2) \times 10^{-22}$

behavior. Aiming to investigate the minimal nanocellulose layer thickness for optimal barrier performance, we measured the OTR of the samples with various deposits thicknesses. The results are shown in Fig. 7a.

The oxygen permeability of PLA(CNF) was stable notwithstanding the number of deposits or the layer thickness. Even very thin films allowed for a high gain in barrier properties. The calculated permeation values of the CS/CNF barrier layer reached $(1.7 \pm 0.1) \times 10^{-22} \text{ m}^3 \cdot \text{m} / \text{m}^2 \cdot \text{s} \cdot \text{Pa}$ for 60 nm (10 deposits). For CNF coatings, an optimal thickness of 20 nm was found, corresponding to 10 layers. These values were taken at the intersection between the extrapolation of the step and flat part of the graph.

Concerning chitosan/CNF TEMPO barrier layer, the O₂ permeation value for 2 deposits is similar to chitosan-coated PLA and the optimum barrier property was obtained with 32 nm, i.e. 8 deposits. The reduced effect of CNF TEMPO coatings compared to CNF coatings is probably due to self-repulsion of the negatively-charged nanofibers. Indeed, TEMPO treatment aims at reducing aggregations, through the limitation of interactions between the nanofibers and thus network density (Fukuzumi et al., 2009). This allowed us to use a more concentrated suspension than for untreated fibers (CNF). After normalization and with 10 deposits of CNF TEMPO the CS/CNF TEMPO barrier layers reached the efficiency of CNF and CNC barrier properties ($(1.9 \pm 0.2) \times 10^{-22} \text{ m}^3 \cdot \text{m} / \text{m}^2 \cdot \text{s} \cdot \text{Pa}$).

Concerning CNC coatings, a steady enhancement in barrier properties was observed when the number of deposits increases from 120 nm (2 deposits) to 360 nm (8 deposits). CNC coated samples can be optimized with a coating of 8 layers, corresponding to a 320 nm thickness.

Normalized permeation values, obtained through Eq. (7), are useful to understand the intrinsic properties of the different coating types; however, the cellulose layer being on average 1000 times thinner than the PLA layer, its influence on the entire barrier properties of the multilayer sample is fairly limited, which explains the important difference between OP(sample) and OP(CS/NC). Both values are relevant.

After normalization, the CS/CNC oxygen permeation values were similar to the CS/CNF coatings values (Table 3), although CNC, CNF and CNF TEMPO have different crystallinities. According to their origin and extraction process, CNC can reach a crystallinity up to 75–90 %, whereas the crystallinity of CNF or CNF TEMPO stay under 65 % (He et al., 2020; Wang et al., 2019). High crystallinity together with the high density and polarity of the nanocelluloses can explain their high oxygen barrier properties. The ability to orient CNC allows them to pack more densely and decreases the oxygen molecule path. To have high efficiency, the minimum layer thickness of CNC is however higher compared to CNF. Compared to literature data, we can also suggest a relationship between CNC orientation and oxygen barrier properties. Du et al. (2021) reached an oxygen transmission rate value about $1 \times 10^{-14} \text{ m}^3 \cdot (\text{STP}) / \text{m}^2 \cdot \text{s} \cdot \text{Pa}$ for very slightly or non-oriented CNC sample, whereas in our study, with a much stronger orientation, this value was approximately 17 times lower (Table 3).

For the sake of comparison, classic PLA/nanocelluloses composites, even with high CNC content, reach permeability values which are mostly in the same order of magnitude as PLA (Espino-Pérez et al., 2013, 2018). For example, the oxygen permeability of amorphous PLA amounting to $(2.7 \pm 0.3) \times 10^{-18} \text{ m}^3 \cdot \text{m} / \text{m}^2 \cdot \text{s} \cdot \text{Pa}$ could be reduced to $(1.7 \pm 0.2) \times 10^{-18} \text{ m}^3 \cdot \text{m} / \text{m}^2 \cdot \text{s} \cdot \text{Pa}$ for PLA/CNC nanocomposites containing 6 wt% CNC (Espino-Pérez et al., 2018) or to $9.2 \times 10^{-19} \text{ m}^3 \cdot \text{m} / \text{m}^2 \cdot \text{s} \cdot \text{Pa}$ in samples containing 50 wt% of CNC (Faraj et al., 2022). This shows that the 2D-multilayer structure is far more efficient for barrier properties than nanocomposite structures.

A drawback of multilayer structures is the high sensibility of the barrier performance to humidity. Therefore, the oxygen permeation measurements were also performed in “dry-humid” and humid environments. “Dry-humid” environment means that humid oxygen is applied to the PLA side of the film and dry nitrogen to the nanocelluloses side, allowing to test the PLA ability to protect the nanocelluloses from water. Fig. 7b illustrates the comparison of oxygen permeability in dry,

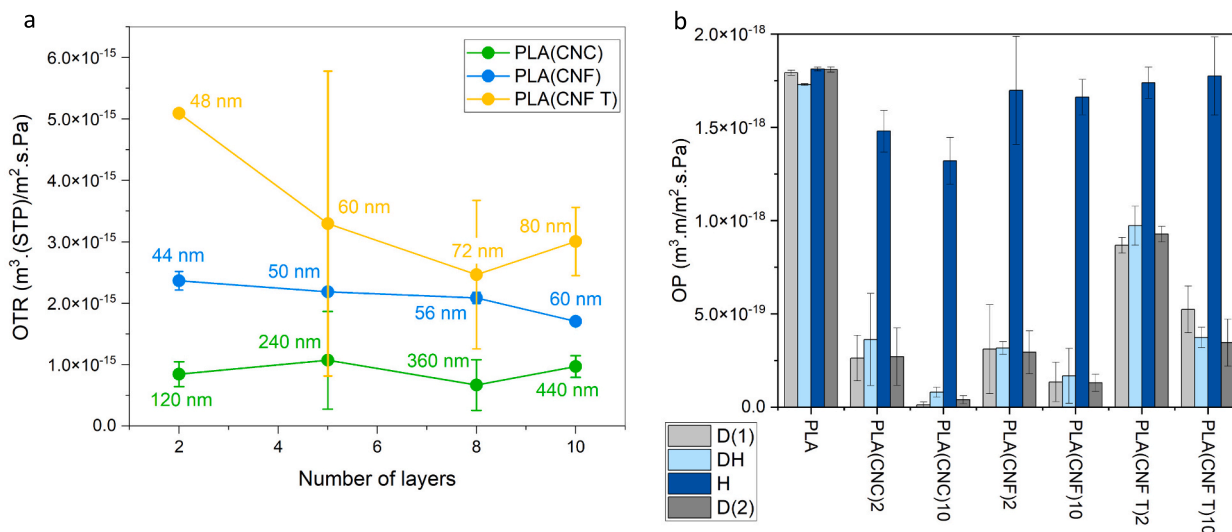


Fig. 7. Oxygen transmission rate (OTR) of coated films as a function of their respective number of nanocellulose layers (with their respective layer thicknesses, in nm) (a) and the comparison of oxygen permeability of coated PLA films in dry (D(1) and D(2)), dry-humid (DH) and humid environment (H) (b).

dry-humid, humid (80 ± 3 %) and dried environment.

An uncoated-PLA film was studied as a blank. As observed in Fig. 7b in dry, dry-humid or humid conditions, the oxygen permeability of PLA remained constant. The same measurements were performed for coated-PLA samples with 2 and 10 layers of nanocelluloses. In dry-humid environment (light blue column in Fig. 7b), small increases in oxygen permeability were noticed, while overall staying close to dry values and well below the oxygen permeability of pure PLA. Hence the use of PLA can protect the nanocellulose layer from water uptake and maintain the oxygen barrier performance.

In order to characterize the resilience of nanocellulose layers, the oxygen permeability of samples was measured at 80 % RH in both side of the permeation cell. Results are reported as dark blue column in Fig. 7b. In that case, as predicted from the measurements of water vapor sorption kinetics (Fig. 6), the O_2 barrier properties were lost. More interestingly, after drying of the films (dried conditions), the nanocelluloses were able to fully recover their properties, since the films reached at 0 % RH the oxygen permeation values they had before (Fig. 7b). These results illustrate the strong resilience of nanocellulose layers regarding their barrier properties.

4. Conclusion

Our starting hypothesis, that a bio-sourced, nanocelluloses-based multilayered packaging material could be designed, is confirmed by this work. It shows the potential of PLA/nanocellulose multilayered films as high water and oxygen barrier materials. Multilayered film built-up was optimized using a chitosan layer in order to increase the compatibility between PLA and nanocellulose and keeping the fully bio-based character of the material. Locally oriented CNC layers were obtained using repeated layer deposition. Furthermore, the optimal coating thickness in terms of oxygen permeability was determined for different types of nanocelluloses: CNC and CNF had almost the same oxygen barrier properties, but the optimum layer thickness of CNC was larger. TEMPO-oxidized CNF were slightly less performing than native CNF. In a dry environment coated-PLA films outperformed PLA/nanocelluloses bulk composites by several orders of magnitude for oxygen barrier, and when nanocellulose layers were shielded by PLA, the samples barrier properties in humid conditions equaled the ones in dry conditions. However, unsurprisingly, without protection at high RH the nanocellulose layers lost their barrier properties. When films were dried again, their barrier performance was however fully restored, which highlights the resilience of nanocelluloses. The water vapor permeability of PLA seems thus low

enough to protect the nanocelluloses from swelling and property loss. These results are of high applicative relevance, because those materials, being formed of thin CNF or oriented CNC films between PLA shielding layers, are fully bio-based polymer films with an oxygen barrier performance higher than that of commonly used ethyl vinyl alcohol materials, even at high humidity. Among the three nanocelluloses types used, CNC are the most efficient because they can form thicker layers. Moreover, they can self-orient locally, as evidenced by AFM coupled to FFT, which gives further optimization potential. CNF coatings have also shown excellent intrinsic barrier properties, although their tendency to aggregate does not allow layer deposition at high concentrations, preventing the fabrication of thick layers. Using TEMPO-oxidized CNF, while reducing the aggregation, unfortunately also reduces the interactions between fibers and hence their barrier properties.

This demonstrates the potential of nanocellulose/PLA multilayers for a fully bio-based high-performance food packaging material over a large range of relative humidities. The impact of the orientation of CNC on barrier properties of films needs however to be investigated further.

Funding

The authors wish to acknowledge the doctoral school ABIES for funding the PhD of Manon Guivier.

CRedit authorship contribution statement

Manon Guivier: Data curation, Formal analysis, Investigation, Writing – original draft. **Giana Almeida:** Conceptualization, Methodology, Supervision, Validation, Writing – review & editing. **Sandra Domenek:** Conceptualization, Funding acquisition, Methodology, Project administration, Supervision, Validation, Writing – review & editing. **Chloé Chevigny:** Conceptualization, Methodology, Supervision, Validation, Writing – review & editing.

Declaration of competing interest

The authors declare that they have no known competing financial interests or personal relationships that could have appeared to influence the work reported in this paper.

Data availability

Data will be made available on request.

Acknowledgements

The authors acknowledge the help of Gilles Gerlot for the contact angle measurements, and the assistance of Jean-Marie Herry and Cyrille Sollogoub for the AFM images.

The authors wish to acknowledge the NanoBio chemistry platform (ICMG UAR 2607) for granting access to the electron microscopy facilities.

Appendix A. Supplementary data

Supplementary data to this article can be found online at <https://doi.org/10.1016/j.carbpol.2023.120761>.

References

- Almeida, G., Domenek, S., & Perré, P. (2020). TransPoly: A theoretical model to quantify the dynamics of water transfer through nanostructured polymer films. *Polymer*, *191*, Article 122256. <https://doi.org/10.1016/j.polymer.2020.122256>
- Aulin, C., Karabulut, E., Tran, A., Wågberg, L., & Lindström, T. (2013). Transparent nanocellulosic multilayer thin films on polylactic acid with tunable gas barrier properties. *ACS Applied Materials & Interfaces*, *5*(15), Article 15. <https://doi.org/10.1021/am401700n>
- Blell, R., Lin, X., Lindström, T., Ankerfors, M., Pauly, M., Felix, O., & Decher, G. (2017). Generating in-plane orientational order in multilayer films prepared by spray-assisted layer-by-layer assembly. *ACS Nano*, *11*(1), Article 1. <https://doi.org/10.1021/acsnano.6b04191>
- Colomines, G., Ducruet, V., Courgneau, C., Guinault, A., & Domenek, S. (2010). Barrier properties of poly(lactic acid) and its morphological changes induced by aroma compound sorption: Barrier properties of PLA and aroma compound sorption. *Polymer International*, *59*(6), 818–826. <https://doi.org/10.1002/pi.2793>
- Courgneau, C., Domenek, S., Lebossé, R., Guinault, A., Avérous, L., & Ducruet, V. (2012). Effect of crystallization on barrier properties of formulated polylactide: Barrier properties of formulated polylactide. *Polymer International*, *61*(2), 180–189. <https://doi.org/10.1002/pi.3167>
- Cranston, E. D., & Gray, D. G. (2006). Formation of cellulose-based electrostatic layer-by-layer films in a magnetic field. *Science and Technology of Advanced Materials*, *7*(4), 319–321. <https://doi.org/10.1016/j.stam.2006.02.007>
- Cranston, E. D., & Gray, D. G. (2008). Birefringence in spin-coated films containing cellulose nanocrystals. *Colloids and Surfaces A: Physicochemical and Engineering Aspects*, *325*(1–2), Article 1–2. <https://doi.org/10.1016/j.colsurfa.2008.04.042>
- Crouvisier-Urien, K., Bodart, P. R., Winckler, P., Raya, J., Gougeon, R. D., Cayot, P., Karbowiak, T., ... (2016). Biobased composite films from chitosan and lignin: Antioxidant activity related to structure and moisture. *ACS Sustainable Chemistry and Engineering*, *4*(12), 6371–6381. <https://doi.org/10.1021/acsschemeng.6b00956>
- Despond, S., Espuche, E., & Domard, A. (2001). Water sorption and permeation in chitosan films: Relation between gas permeability and relative humidity. *Journal of Polymer Science Part B: Polymer Physics*, *39*(24), 3114–3127. <https://doi.org/10.1002/polb.10064>
- Du, L., Yu, H., Zhang, B., Tang, R., Zhang, Y., Qi, C., Wolcott, M. P., Yu, Z., & Wang, J. (2021). Transparent oxygen barrier nanocellulose composite films with a sandwich structure. *Carbohydrate Polymers*, *268*, Article 118206. <https://doi.org/10.1016/j.carbpol.2021.118206>
- Du, L., Yu, Z., Wang, J., Wolcott, M. P., Zhang, Y., & Qi, C. (2020). Analyzing the film formation mechanism of cellulose nanoparticles (CNPs) based on the fast freeze-drying morphology. *Cellulose*, *27*(12), 6921–6933. <https://doi.org/10.1007/s10570-020-03164-z>
- Espino-Pérez, E., Bras, J., Almeida, G., Plessis, C., Belgacem, N., Perré, P., & Domenek, S. (2018). Designed cellulose nanocrystal surface properties for improving barrier properties in polylactide nanocomposites. *Carbohydrate Polymers*, *183*, 267–277. <https://doi.org/10.1016/j.carbpol.2017.12.005>
- Espino-Pérez, E., Bras, J., Almeida, G., Relkin, P., Belgacem, N., Plessis, C., & Domenek, S. (2016). Cellulose nanocrystal surface functionalization for the controlled sorption of water and organic vapours. *Cellulose*, *23*(5), 2955–2970. <https://doi.org/10.1007/s10570-016-0994-y>
- Espino-Pérez, E., Bras, J., Ducruet, V., Guinault, A., Dufresne, A., & Domenek, S. (2013). Influence of chemical surface modification of cellulose nanowhiskers on thermal, mechanical, and barrier properties of poly(lactide) based bionanocomposites. *European Polymer Journal*, *49*(10), 3144–3154. <https://doi.org/10.1016/j.eurpolymj.2013.07.017>
- Faraj, H., Follain, N., Sollogoub, C., Almeida, G., Chappey, C., Marais, S., Tencé-Girault, S., Gouanvé, F., Espuche, E., & Domenek, S. (2022). Gas barrier properties of polylactide/cellulose nanocrystals nanocomposites. *Polymer Testing*, *113*, Article 107683. <https://doi.org/10.1016/j.polymertesting.2022.107683>
- Ferrer, A., Pal, L., & Hubbe, M. (2017). Nanocellulose in packaging: Advances in barrier layer technologies. *Industrial Crops and Products*, *95*, 574–582. <https://doi.org/10.1016/j.indcrop.2016.11.012>
- Fortunati, E., Peltzer, M., Armentano, I., Torre, L., Jiménez, A., & Kenny, J. M. (2012). Effects of modified cellulose nanocrystals on the barrier and migration properties of PLA nano-biocomposites. *Carbohydrate Polymers*, *90*(2), 948–956. <https://doi.org/10.1016/j.carbpol.2012.06.025>
- Fukuzumi, H., Saito, T., Iwata, T., Kumamoto, Y., & Isogai, A. (2009). Transparent and high gas barrier films of cellulose nanofibers prepared by TEMPO-mediated oxidation. *Biomacromolecules*, *10*(1), Article 1. <https://doi.org/10.1021/bm801065u>
- Gicquel, E., Martin, C., Garrido Yanez, J., & Bras, J. (2017). Cellulose nanocrystals as new bio-based coating layer for improving fiber-based mechanical and barrier properties. *Journal of Materials Science*, *52*(6), Article 6. <https://doi.org/10.1007/s10853-016-0589-x>
- He, Y., Boluk, Y., Pan, J., Ahniyaz, A., Deltin, T., & Claesson, P. M. (2020). Comparative study of CNC and CNF as additives in waterborne acrylate-based anti-corrosion coatings. *Journal of Dispersion Science and Technology*, *41*(13), 2037–2047. <https://doi.org/10.1080/01932691.2019.1647229>
- Herrera, M. A., Sirviö, J. A., Mathew, A. P., & Oksman, K. (2016). Environmental friendly and sustainable gas barrier on porous materials: Nanocellulose coatings prepared using spin- and dip-coating. *Materials & Design*, *93*, 19–25. <https://doi.org/10.1016/j.matdes.2015.12.127>
- Hubbe, M. A., Ferrer, A., Tyagi, P., Yin, Y., Salas, C., Pal, L., & Rojas, O. J. (2017). Nanocellulose in thin films, coatings, and plies for packaging applications: A review. *BioResources*, *12*(1), Article 1. <https://doi.org/10.15376/biores.12.1.2143-2233>
- Islam, M. T., Alam, M. M., Patrucco, A., Montarsolo, A., & Zoccola, M. (2014). Preparation of nanocellulose: A review. *AATCC Journal of Research*, *1*(5), 17–23. <https://doi.org/10.14504/ajr.1.5.3>
- Jiménez Saelices, C., & Capron, I. (2018). Design of Pickering Micro- and Nanoemulsions Based on the structural characteristics of nanocelluloses. *Biomacromolecules*, *19*(2), 460–469. <https://doi.org/10.1021/acs.biomac.7b01564>
- Jung, B. N., Jung, H. W., Kang, D. H., Kim, G. H., Lee, M., Shim, J. K., & Hwang, S. W. (2020). The fabrication of flexible and oxygen barrier cellulose nanofiber/polylactic acid nanocomposites using cosolvent system. *Journal of Applied Polymer Science*, *137*(47), 49536. <https://doi.org/10.1002/app.49536>
- Koppolu, R., Lahti, J., Abitbol, T., Swerin, A., Kuusipalo, J., & Toivakka, M. (2019). Continuous processing of nanocellulose and polylactic acid into multilayer barrier coatings. *ACS Applied Materials & Interfaces*, *11*(12), Article 12. <https://doi.org/10.1021/acsaami.9b00922>
- Lagaron, J. M., Cabedo, L., Cava, D., Feijoo, J. L., Gavara, R., & Gimenez, E. (2005). Improving packaged food quality and safety. Part 2: Nanocomposites. *Food Additives and Contaminants*, *22*(10), 994–998. <https://doi.org/10.1080/02652030500239656>
- Lange, J., & Wyser, Y. (2003). Recent innovations in barrier technologies for plastic packaging? a review. *Packaging Technology and Science*, *16*(4), Article 4. <https://doi.org/10.1002/pts.621>
- Lavoine, N., Desloes, I., Dufresne, A., & Bras, J. (2012). Microfibrillated cellulose – its barrier properties and applications in cellulosic materials: A review. *Carbohydrate Polymers*, *90*(2), 735–764. <https://doi.org/10.1016/j.carbpol.2012.05.026>
- Le Gars, M., Bras, J., Salmi-Mani, H., Ji, M., Dragoe, D., Faraj, H., Domenek, S., Belgacem, N., & Roger, P. (2020). Polymerization of glycidyl methacrylate from the surface of cellulose nanocrystals for the elaboration of PLA-based nanocomposites. *Carbohydrate Polymers*, *234*, Article 115899. <https://doi.org/10.1016/j.carbpol.2020.115899>
- Le Gars, M., Dhuiège, B., Delvart, A., Belgacem, M. N., Missoum, K., & Bras, J. (2020). High-barrier and antioxidant poly(lactic acid)/nanocellulose multilayered materials for packaging. *ACS Omega*, *5*(36), Article 36. <https://doi.org/10.1021/acsomega.0c01955>
- Li, Q., Zhou, J., & Zhang, L. (2009). Structure and properties of the nanocomposite films of chitosan reinforced with cellulose whiskers. *Journal of Polymer Science Part B: Polymer Physics*, *47*(11), 1069–1077. <https://doi.org/10.1002/polb.21711>
- Lin, N., & Dufresne, A. (2014). Nanocellulose in biomedicine: Current status and future prospect. *European Polymer Journal*, *59*, 302–325. <https://doi.org/10.1016/j.eurpolymj.2014.07.025>
- Lu, P., Guo, M., Xu, Z., & Wu, M. (2018). Application of nanofibrillated cellulose on BOPP/LDPE film as oxygen barrier and antimicrobial coating based on cold plasma treatment. *Coatings*, *8*(6), 207. <https://doi.org/10.3390/coatings8060207>
- Martin, C., & Jean, B. (2014). Nanocellulose/polymer multilayered thin films: Tunable architectures towards tailored physical properties. *Nordic Pulp & Paper Research Journal*, *29*(1), Article 1. <https://doi.org/10.3183/npprj-2014-29-01-p019-030>
- Mirmehdi, S., Hein, P. R. G., de Luca Sarantopoulos, C. I. G., Dias, M. V., & Tonoli, G. H. D. (2018). Cellulose nanofibrils/nanoclay hybrid composite as a paper coating: Effects of spray time, nanoclay content and corona discharge on barrier and mechanical properties of the coated papers. *Food Packaging and Shelf Life*, *15*, 87–94. <https://doi.org/10.1016/j.fpsl.2017.11.007>
- Mujica-García, A., Hooshmand, S., Skrifvars, M., Kenny, J. M., Oksman, K., & Peponi, L. (2016). Poly(lactic acid) melt-spun fibers reinforced with functionalized cellulose nanocrystals. *RSC Advances*, *6*(11), 9221–9231. <https://doi.org/10.1039/C5RA22818B>
- Nair, S. S., Zhu, J., Deng, Y., & Ragauskas, A. J. (2014). High performance green barriers based on nanocellulose. *Sustainable Chemical Processes*, *2*(1), Article 1. <https://doi.org/10.1186/s40508-014-0023-0>
- Nazari, B., Kumar, V., Bousfield, D. W., & Toivakka, M. (2016). Rheology of cellulose nanofibers suspensions: Boundary driven flow. *Journal of Rheology*, *60*(6), 1151–1159. <https://doi.org/10.1122/1.4960336>
- Pignon, F., Challamel, M., De Geyer, A., Elchamaa, M., Semeraro, E. F., Hengl, N., Jean, B., Putaux, J.-L., Gicquel, E., Bras, J., Prevost, S., Sztucki, M., Narayanan, T., & Djeridi, H. (2021). Breakdown and buildup mechanisms of cellulose nanocrystal suspensions under shear and upon relaxation probed by SAXS and SALS. *Carbohydrate Polymers*, *260*, Article 117751. <https://doi.org/10.1016/j.carbpol.2021.117751>
- Qing, Y., Sabo, R., Zhu, J. Y., Agarwal, U., Cai, Z., & Wu, Y. (2013). A comparative study of cellulose nanofibrils disintegrated via multiple processing approaches.

- Carbohydrate Polymers*, 97(1), Article 1. <https://doi.org/10.1016/j.carbpol.2013.04.086>
- Revol, J.-F., Bradford, H., Giasson, J., Marchessault, R. H., & Gray, D. G. (1992). Helicoidal self-ordering of cellulose microfibrils in aqueous suspension. *International Journal of Biological Macromolecules*, 14(3), 170–172. [https://doi.org/10.1016/S0141-8130\(05\)80008-X](https://doi.org/10.1016/S0141-8130(05)80008-X)
- Rocca-Smith, J. R. (2016). Impact of corona treatment on PLA film properties. *Polymer Degradation and Stability*, 8.
- Spence, K. L., Venditti, R. A., Rojas, O. J., Habibi, Y., & Pawlak, J. J. (2011). A comparative study of energy consumption and physical properties of microfibrillated cellulose produced by different processing methods. *Cellulose*, 18(4), 1097–1111. <https://doi.org/10.1007/s10570-011-9533-z>
- Spieser, H., Denneulin, A., Deganello, D., Gethin, D., Koppolu, R., & Bras, J. (2020). Cellulose nanofibrils and silver nanowires active coatings for the development of antibacterial packaging surfaces. *Carbohydrate Polymers*, 240, Article 116305. <https://doi.org/10.1016/j.carbpol.2020.116305>
- Ssekatawa, K., Byarugaba, D. K., Wampande, E. M., Moja, T. N., Nxumalo, E., Maaza, M., Sackey, J., Ejobi, F., & Kirabira, J. B. (2021). Isolation and characterization of chitosan from ugandan edible mushrooms, Nile perch scales and banana weevils for biomedical applications. *Scientific Reports*, 11(1), 4116. <https://doi.org/10.1038/s41598-021-81880-7>
- Szymańska-Chargot, M., Chylińska, M., Pieczywek, P. M., Walkiewicz, A., Pertile, G., Fraç, M., Cieślak, K. J., & Zdunek, A. (2020). Evaluation of nanocomposite made of polylactic acid and nanocellulose from carrot pomace modified with silver nanoparticles. *Polymers*, 12(4), 812. <https://doi.org/10.3390/polym12040812>
- Thomas, B., Raj, M. C., B. A. K., H. R. M., Joy, J., Moores, A., Drisko, G. L., & Sanchez, C. (2018). Nanocellulose, a versatile green platform: From biosources to materials and their applications. *Chemical Reviews*, 118(24), Article 24. <https://doi.org/10.1021/acs.chemrev.7b00627>
- Thomas, P., Duolikun, T., Rumjit, N. P., Moosavi, S., Lai, C. W., Bin Johan, M. R., & Fen, L. B. (2020). Comprehensive review on nanocellulose: Recent developments, challenges and future prospects. *Journal of the Mechanical Behavior of Biomedical Materials*, 110, Article 103884. <https://doi.org/10.1016/j.jmbbm.2020.103884>
- Toivonen, M. S., Kurki-Suonio, S., Schacher, F. H., Hietala, S., Rojas, O. J., & Ikkala, O. (2015). Water-resistant, transparent hybrid nanopaper by physical cross-linking with chitosan. *Biomacromolecules*, 16(3), 1062–1071. <https://doi.org/10.1021/acs.biomac.5b00145>
- Vanden Braber, N. L., Díaz Vergara, L. I., Morán Vieyra, F. E., Borsarelli, C. D., Yossen, M. M., Vega, J. R., Correa, S. G., & Montenegro, M. A. (2017). Physicochemical characterization of water-soluble chitosan derivatives with singlet oxygen quenching and antibacterial capabilities. *International Journal of Biological Macromolecules*, 102, 200–207. <https://doi.org/10.1016/j.ijbiomac.2017.04.028>
- Vartiainen, J., Shen, Y., Kaljunen, T., Malm, T., Vähä-Nissi, M., Putkonen, M., & Harlin, A. (2016). Bio-based multilayer barrier films by extrusion, dispersion coating and atomic layer deposition. *Journal of Applied Polymer Science*, 133(2), Article 2. <https://doi.org/10.1002/app.42260>
- Wang, L., Chen, C., Wang, J., Gardner, D. J., & Tajvidi, M. (2020). Cellulose nanofibrils versus cellulose nanocrystals: Comparison of performance in flexible multilayer films for packaging applications. *Food Packaging and Shelf Life*, 23, Article 100464. <https://doi.org/10.1016/j.fpsl.2020.100464>
- Wang, X., Chang, C. H., Jiang, J., Liu, Q., Liao, Y., Lu, J., Li, L., Liu, X., Kim, J., Ahmed, A., Nel, A. E., & Xia, T. (2019). The crystallinity and aspect ratio of cellulose nanomaterials determine their pro-inflammatory and immune adjuvant effects in vitro and in vivo. *Small*, 15(42), Article 1901642. <https://doi.org/10.1002/smll.201901642>
- Yook, S., Park, H., Park, H., Lee, S.-Y., Kwon, J., & Youn, H. J. (2020). Barrier coatings with various types of cellulose nanofibrils and their barrier properties. *Cellulose*, 27(8), Article 8. <https://doi.org/10.1007/s10570-020-03061-5>
- Yoshiharu, N., Shigenori, K., Masahisa, W., & Takeshi, O. (1997). Cellulose microcrystal film of high uniaxial orientation. *Macromolecules*, 30(20), 6395–6397. <https://doi.org/10.1021/ma970503y>